A Compact Large-Current Equalizer Based on Flyback Conversion for Large-Scale Battery Packs

Shiquan Liu, Yue Wang, *Graduate Student Member, IEEE*, Shiyu Wang, Wenyuan Zhao,
and Yunlong Shang, *Member, IEEE*

***Abstract*—The equalizer can greatly improve the consistency of the series-connected battery string, which has been widely used in the field of electric vehicles. However, the existing equalization topology suffers from the disadvantages of slow equalization, large size, and complex control. Therefore, a compact equalization topology is proposed based on flyback conversion. Distinguishing from the traditional flyback conversion topology, the proposed equalizer divides the series-connected battery cells into odd and even groups. The neighboring battery cells share a pair of MOSFETs, which greatly reduces the number of switches and costs. Moreover, the proposed equalizer has both equalization and charge equalization modes, which can be flexibly applied in different situations. An experimental prototype is designed for 12-cell large-capacity batteries. The experimental results show that the peak equalization current reaches 10 A, which is five times higher than the traditional active equalization topology. The voltage difference is less than 5 mV after equalization. Compared with the existing equalization topologies, the proposed equalizer has a smaller size, faster equalization speed, and optional equalization modes, which can be applied to large-scale battery pack scenarios.**

***Index Terms*—Battery equalization, flyback converter, transformer.**

I. INTRODUCTION

As THE energy problem becomes more and more prominent, all fields are pursuing energy efficiency and environmental protection [1]. Due to the advantages of high energy density and long cycle life, lithium-ion batteries are being widely used in the field of energy storage and electric vehicles [2], [3], [4]. However, the quality of lithium-ion batteries is not easy to control in mass production, which leads to slight differences as they leave the factory. More seriously, the inconsistency in batteries is magnified when thousands of batteries are used in series [5], [6], [7], [8]. Specifically, the charging and discharging process of the battery will be affected. When a certain cell reaches the threshold voltage, the charging or discharging process of the whole battery pack will be terminated [9]. Furthermore, the inconsistency will become more and more obvious in use with the change in the environment. Finally, the efficiency, service life, and usable capacity of the battery pack will decrease and even cause a thermal runaway explosion [10], [11]. Therefore, battery equalization is particularly important.

Equalization topologies have received widespread attention. Existing equalization circuits are mainly divided into passive and active equalization based on whether has energy dissipation or not [12], [13], [14], [15]. Passive equalization releases excess energy by discharging the cell in parallel with a resistor. Due to the advantages of simple structure, easy control, and small size, passive equalization has become the mainstream equalization method at present. However, passive equalization suffers from serious energy waste during use, where energy is consumed through the resistance rather than being stored or converted. In contrast, the active equalization circuit can redistribute energy between the series-connected battery cells without energy waste, which is a much more efficient method.

According to the different equalization strategies, active equalization can be divided into state of charge (SOC)-based equalization and voltage-based equalization [16]. Equalization based on SOC provides a more rational distribution of the battery energy. However, it is difficult to accurately estimate SOC because the battery charging and discharging process is nonlinear and easily affected by temperature, and other factors. Compared to SOC, the voltage of the battery is a much easier parameter to measure. Therefore, voltage-based equalization is easier to implement in practical applications.

According to the energy conversion device, active equalization can be classified as capacitor-based [17], [18], [19], [20], inductor-based [21], [22], [23], [24], and transformer-based equalization [15], [25], [26], [27], [28], [29], [30], [31], [32]. Chen et al. [19] proposed an equalizer using two capacitors along with a resistor. This equalizer achieves the effect of charging when the capacitor is in series and discharging when it is in parallel by changing the capacitor series or parallel state, which has the advantages of simple circuit structure and high reliability. However, the state of the capacitor needs to be changed all the time during the battery pack balancing, which reduces the speed of equalization, and the circuit works at a lower switching frequency which results in a larger circuit volume. Shang et al. [20] proposed an automatic switched-coupling-capacitor equalizer, which achieves automatic equalization between cells without

---

Received 24 June 2024; revised 26 August 2024; accepted 13 October 2024. Date of publication 16 October 2024; date of current version 12 December 2024. This work was supported in part by the National Natural Science Foundation of China under Grant 62122041, Grant 62173211, and Grant 62333013, and in part by the Natural Science Foundation of Shandong Province, China, under Grant ZR2021JQ25. Recommended for publication by Associate Editor M. Hagiwara. *(Corresponding author: Yunlong Shang.)*

The authors are with the School of Control Science and Engineering, Shandong University, Jinan 250061, China (e-mail: 202234100@mail.sdu.edu.cn; moonwang@mail.sdu.edu.cn; shiyuwang@mail.sdu.edu.cn; zhaowenyuan@mail.sdu.edu.cn; yshang@sdu.edu.cn).

Color versions of one or more figures in this article are available at https://doi.org/10.1109/TPEL.2024.3482463.

Digital Object Identifier 10.1109/TPEL.2024.3482463

the need for additional voltage monitoring circuits. All cells and modules can share a single converter in the equalizer. Therefore, it has a distinct advantage that is small in size. Nevertheless, the low balancing current, results in a long equalization time, which is difficult to apply to large-scale battery packs. Ding et al. [23] proposed a novel active equalization topology, which is based on the traditional Buck–Boost circuit with a two-stage hierarchical architecture. However, the energy exchange is only between adjacent batteries. Specifically, it is unable to directly transfer the energy from the high-voltage cell to the low-voltage cell arbitrarily, making a lower equalization speed. Moreover, the two-stage hierarchical architecture uses more inductive devices and MOSFETs, leading to a large circuit size and high cost, making it difficult to apply. Lu et al. [24] proposed a novel inductor-based nondissipative equalizer, which replaces part of the energy storage inductors with MOSFETs. Compared to the traditional multiple switch-inductors equalizer, it reduces the number of inductors by about 50%. However, the decrease of the energy storage element leads to an increase in the equalization time. Also, more MOSFETs are used, leading to a larger circuit loss.

Unlike capacitor-based and inductor-based equalization, transformer-based equalization circuit has the advantages of simple control, easy isolation, and high efficiency. Kim et al. [29] proposed a modularized two-stage charge equalizer, which uses a two-stage dc–dc isolation converter to reduce the voltage stress on the electrical components. However, each cell unit requires four pairs of MOSFETs in the equalizer, and the two-stage architecture leads to a large circuit size. Therefore, Li et al. [30] proposed a high-efficiency active battery-balancing circuit using a multiwinding transformer, which realizes energy exchange from any cell to any cell through a symmetrical multiwinding transformer. Each cell only needs one MOSFET and one capacitor achieving efficient equalization. However, for long battery strings, multiwinding transformers are complicated to design and difficult to match between different windings. Shang et al. [31] proposed a modularization method using multiwinding transformers for battery equalizers, which divides series-connected batteries into different modules. Intramodule batteries are equalized using forward conversion and intermodule batteries using flyback conversion. In addition, this equalizer realizes automatic equalization without extra voltage monitoring circuits. Nevertheless, the multiwinding transformer leads to complex circuit design, large size, and high cost.

The flyback converter is noteworthy for its natural electrical isolation, superior electrical performance, and control flexibility, which has great potential in the equalization area. As shown in Fig. 1, Yu et al. [32] proposed a multicell-to-multicell equalizer, which is based on the flyback conversion. Two pairs of MOSFET switches are equipped for each cell. By controlling the ON-OFF state of the MOSFETs, different batteries can be charged or discharged through a common transformer. However, the equalization circuit requires a large number of MOSFETs. In short, it is still challenging to achieve a balance of small size, low cost, and high speed. To address the above problems, a small size and large current equalizer suitable for large battery packs is proposed in this article. By sharing the MOSFET array, neighboring battery cells can share a pair of switches. Compared to [32], the power devices are halved overall. However, the equivalent circuit does not change during a single equalization process, as shown in Fig. 4. By rationally designing the flyback converter parameters, the equalizer can continuously charge and discharge the cell with a large current throughout the equalization process.

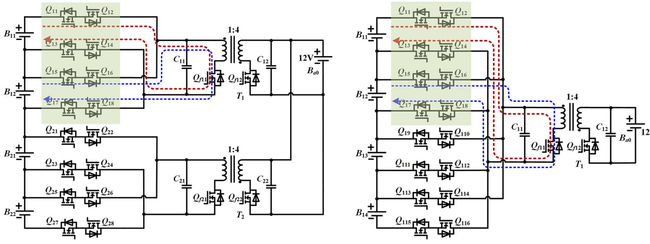

(a) (b)

Fig. 1. Multicell-to-multicell equalizer based on flyback conversion [32]. (a) One module. (b) Two modules.

This article has three main contributions. First, compared with the traditional flyback converter topology, the proposed equalizer reduces by about 50% MOSFETs, leading to a low cost and small size. Second, by rationally designing the flyback converter circuit, large-current equalization is ensured. The equalization current is five times larger than the traditional active equalization topology, which is more suitable for large battery packs. Finally, the proposed equalizer provides selectable operating modes, not only in pure equalization mode (Mode I) but also in charging equalization mode (Mode II). The dual-purpose machine design enables the equalizer to be suitable for more diverse application scenarios.

The rest of this article is organized as follows. Section II presents the fundamentals of the proposed equalization topology. Section III analyzes the design process of the flyback converter. Section IV verifies the effectiveness of the equalizer. The various existing equalization topologies are compared in Section V. Finally, Section VI concludes this article.

II. PROPOSED EQUALIZER

A. Circuit Structure of Proposed Equalizer

Fig. 2(a) illustrates the equalization topology, which contains twelve batteries B_i ($i = 1, \ldots, 12$). All twelve batteries are divided into two groups (P_1 and P_2). The odd group (P_1) includes batteries B_1, B_3, B_5, B_7, B_9, and B_{11}. The even group (P_2) includes batteries B_2, B_4, B_6, B_8, B_{10}, and B_{12}. The batteries in P_1 are equalized by transformer T_1. Similarly, the batteries in P_2 are equalized by transformer T_2. The MOSFETs on the primary branch of the transformer can be shared by two neighboring batteries. For example, Q_{21} and Q_{22} are shared by B_1 and B_2. Fig. 2(b) illustrates the equalization topology for n series-connected battery cells. The added cells only need to be attached to the T_1 or T_2 ends through a pair of MOSFETs. From the topology, the positive and negative terminals of the long battery string are linked to the high-voltage terminals of the battery charger through a pair of relays. The primary side of the transformer is attached to the batteries and the secondary side

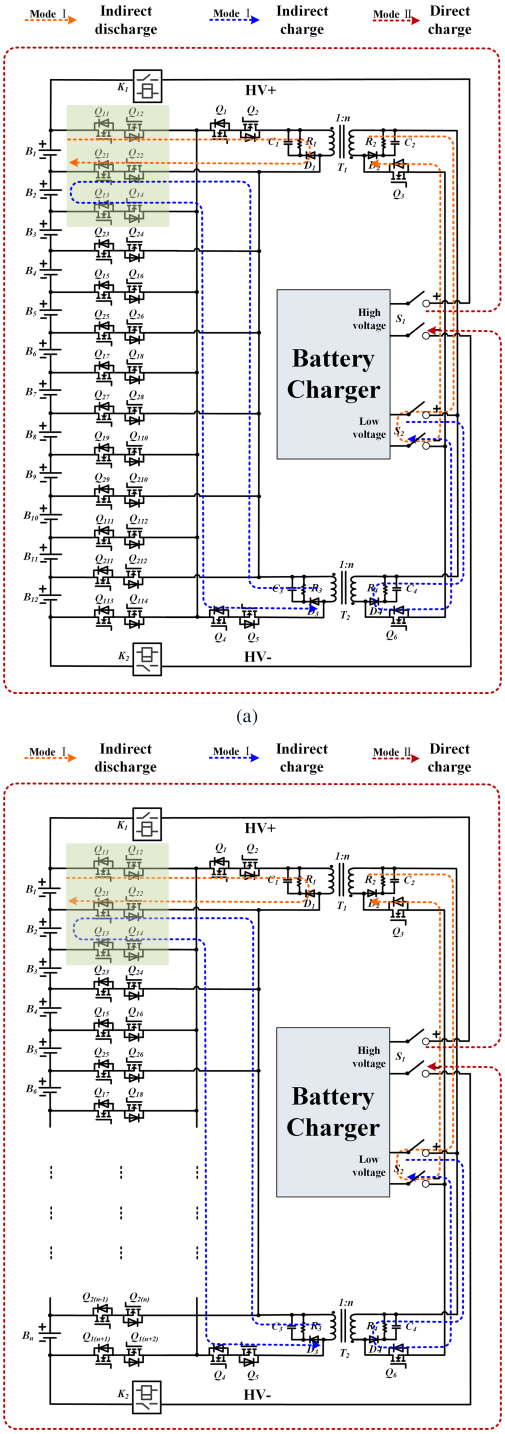

(a)

(b)

Fig. 2. Proposed equalization topology based on the flyback converter. (a) For twelve cells. (b) For *n* cells.

is attached to the low-voltage terminals of the battery charger. This circuit structure is expandable and more suitable for long battery strings.

B. Equalization Strategy

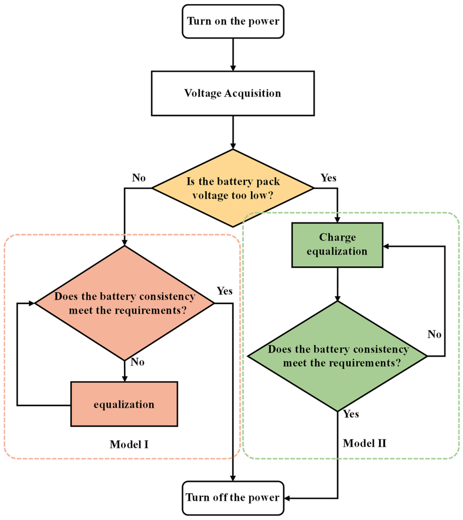

Fig. 3. Circuit working flow chart.

The circuit topology is based on 12 batteries. The circuit working flow chart is shown in Fig. 3. First, the cell voltage is obtained according to the sampling circuit. Then depending on the cell voltage status, the circuit will work in different modes. Specifically, the two operating modes are as follows.

Mode I:

When the initial voltage of the battery cell is high without additional charging, only the battery consistency is poor, the circuit will work in mode I (equalization). The battery cells are connected to the low-voltage terminals of the battery charger through the flyback converter for charging or discharging. The specific steps are as follows.

1) Collect the voltage of 12 batteries, i.e., V_{i} (i = 1, 2 ..., 11, 12), and calculate the average voltage, i.e., V_{aver}.
2) Calculate the voltage difference between each cell and V_{aver}, i.e., V_{dif}, $V_{\mathrm{dif}} = V_{\mathrm{i}} - V_{\mathrm{aver}}$. The maximum positive voltage of V_{dif} is recorded as V_{max1}. The maximum negative voltage of V_{dif} is recorded as V_{max2}.
3) If $V_{\mathrm{max1}} > V_{\mathrm{max2}}$, the corresponding MOSFETs are driven for indirect discharge, as shown by the orange dotted line in Fig. 2. If $V_{\mathrm{max1}} < V_{\mathrm{max2}}$, the cell is charged indirectly, as shown by the blue dotted line in Fig. 2.
4) When the differential voltage between cells is less than 5 mV, the equalization is ended.

Mode II:

When the voltage of the series-connected battery pack is low, the circuit works in mode II (charge equalization). The battery pack is first charged directly through the high-voltage terminals of the battery charger, as shown by the red dotted line in Fig. 2. When the voltage of a cell in the battery pack reaches the charging threshold voltage, the high-voltage circuit is cut off. The battery cell is then connected to the low-voltage terminal of the battery charger for charging through the flyback converter until the voltage of all battery cells reaches the charging threshold voltage.

C. Operation Principles

Figs. 4 and 5, respectively, illustrate the equivalent circuits of the discharging and charging processes for a single battery cell.

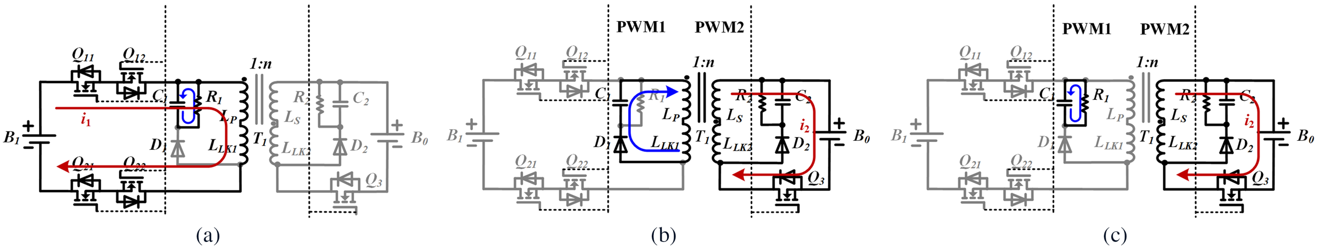

(a) (b) (c)

Fig. 4. Battery cell discharge equivalent circuit diagram. (a) State I. (b) State II. (c) State III.

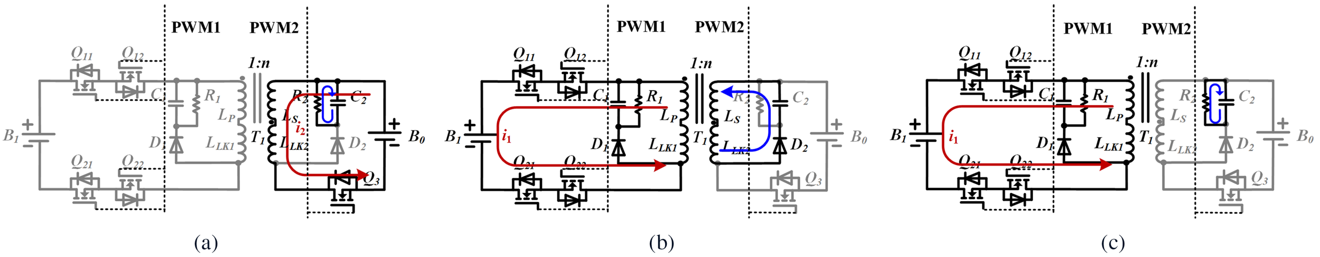

(a) (b) (c)

Fig. 5. Battery cell charge equivalent circuit diagram. (a) State I. (b) State II. (c) State III.

The equivalent circuit contains a cell B_1, a 12 V voltage source B_0, a transformer T_1, two resistance-capacitance-diode (RCD) absorber circuits, and five MOSFETs. The primary side winding inductance can be seen as consisting of an ideal transformer primary inductance L_{P} and a leakage inductance L_{LK1} in series.

Similarly, the secondary side winding inductance consists of the L_{S} and L_{LK2} in series. During the equalization process, the circuit state can be easily controlled with a pair of pulsewidth modulation (PWM) signals. Comparing the charging and discharging in equalization, it is easy to see the two processes are symmetrical and opposite. The only difference is that the energy flows in the opposite direction.

The following descriptions and assumptions are made about the key parameters in the equalization process.

1) The two transformers of T_1 and T_2 have the same number of turns ratio, excitation inductance, leakage inductance, and equivalent resistance.
2) Specify that the current flowing from the primary side of the transformer to cell B_1 is positive. The current flowing from the secondary side to cell B_0 is positive.
3) PWM1 and PWM2 are the MOSFET drive signal outputs. PWM+ drives the MOSFET turning ON. PWM- drives the MOSFET turning OFF. The specific waveform is shown in Fig. 6.

The charging and discharging principles of the cell are similar. To better analyze the equalization circuit, B_1 charging is illustrated as an example. During the steady charging of B_1, four main stages exist in a switching cycle (t_0–t_4). Fig. 6 illustrates the theoretical waveforms of the voltage and current. V_{L1} and V_{L2} are, respectively, the voltages on the primary and secondary sides of the transformer. V_{c2} is the voltage across the absorbing capacitor. V_{ds} is the drain-source voltage of the MOSFET. i_1 and i_2 are respectively the currents flowing through the primary and secondary sides of the transformer.

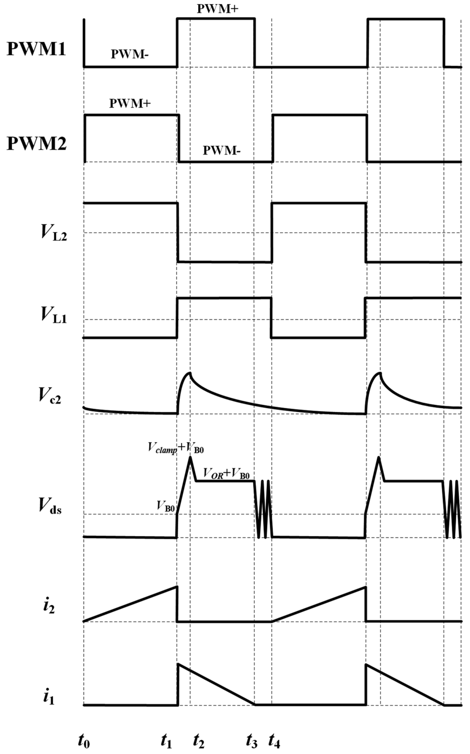

Fig. 6. Key waveforms of voltage and current.

State I (t_0–t_1): At the moment of t_0, the primary side switches Q_{11}, Q_{12}, Q_{21}, and Q_{22} keep OFF. The secondary side switch Q_3 keeps ON.

As shown in Fig. 5(a), a pair of PWM signals is applied to the switch, where PWM+ drives the secondary side switch to turn ON. When Q_3 turns ON, the secondary side of the transformer generates an induced electromotive force, which is approximately equal to the supply voltage B_0. The direction is "positive up and negative down". According to the principle of electromagnetic induction, the primary side of the transformer generates an induced electromotive force in the opposite direction, whose direction is "positive down and negative up". Based on the turns ratio of the transformer, the value of the primary side voltage is

$$V_{L1} = -\frac{V_{B0}}{\mathrm{n}} \tag{1}$$

where V_{B0} is the low voltage supply from the battery charger, and *n* is the transformer turns ratio.

At this moment, the primary side is open without the current path. The secondary side current rises linearly from zero by the transformer inductor coil. The rate of change can be expressed as

$$\frac{di_2}{dt} = \frac{V_{L2}}{L_S} \tag{2}$$

where V_{L2} is the voltage across the secondary side inductor coil and L_{S} is the secondary side excitation inductance.

The secondary side peak current is

$$i_{2\max} = \frac{V_{L2}}{L_S} \cdot (t_1 - t_0)\,. \tag{3}$$

As the current gradually increases, the flux in the core of the transformer gradually increases. The increased magnetic flux can be expressed as

$$\Delta\Phi_+ = \frac{V_{L2}}{N_1} \cdot (t_1 - t_0) \tag{4}$$

where N_1 is the number of turns on the primary side of the transformer.

The external power supply B_0 releases energy to the transformer. The electrical energy is stored as magnetic energy in the secondary winding inductance L_{S} and leakage inductance L_{LK2}. The magnitude of the stored energy can be expressed as

$$Q_{L_S} = \frac{1}{2} L_S I_{L_{SK}}^2 \tag{5}$$

$$Q_{L_{LK2}} = \frac{1}{2} L_{LK2} I_{L_{LK2K}}^2 \tag{6}$$

where I_{LSK} and I_{LLK2K} are the peak currents on the secondary side of the transformer. L_{S} and L_{LK2} are the excitation inductance and leakage inductance on the secondary side.

During the current build-up on the secondary side of the transformer, the energy stored in the absorption capacitor will release energy through the absorber resistor. Since the MOSFET ON-resistance is very small, the drain-source voltage V_{ds} is approximately zero during the secondary side conducts.

State II (t_1 - t_2): At the moment of t_1, the primary side switches Q_{11}, Q_{12}, Q_{21}, and Q_{22} keep ON. The secondary side switch Q_3 keeps OFF.

As shown in Fig. 5(b), PWM- drives the secondary side switch to turn OFF. At the moment when the secondary side of the transformer is disconnected, the secondary side induces an induced electromotive force whose direction is "positive down and negative up" according to the principle of electromagnetic induction. At the same time, the primary side induces an electromotive force in the opposite direction, whose direction is "positive up and negative down". The magnetic energy stored in the transformer is released to the battery cell B_1 starting to charge.

In this case, the energy stored in the excitation inductance L_{S} can be transferred to the primary side after the switch is turned OFF, while the energy stored in the leakage inductance L_{LK2} cannot be transferred to the primary side. When Q_3 turns OFF, the secondary side leakage current first charges the parasitic capacitor C_{DS} on D-S of the MOSFET, causing the voltage V_{ds} to rise from zero to V_{B0}. When D_2 conducts, the energy stored in the leakage inductance is released into capacitor C_2, causing the voltage V_{C2} to rise rapidly across capacitor C_2. At the same time, the voltage V_{ds} rises quickly, which can be expressed as

$$V_{\mathrm{ds}} = V_{C_{\mathrm{lamp}}} + V_{B0} \tag{7}$$

where V_{Clamp} is the capacitor voltage.V_{B0} is the external supply voltage on the secondary side of the transformer.

The secondary side current i_2 drops rapidly to zero at the moment of t_1. As the primary side conducts, the current is then renewed through the primary side. The primary side current i_1 begins to gradually decrease from the maximum value.

State III (t_2 - t_3): The primary side switches keep on and the secondary side switch keeps OFF.

At the moment of t_2, all of the energy in the leakage inductance is transferred to the absorption capacitor C_2. As shown in Fig. 5(c), the primary side current continues to decrease gradually from the maximum value. The maximum value of the current when it starts to decrease can be expressed as

$$i_{1\max} = \frac{V_{L1}}{L_P} \cdot (t_3 - t_1) \tag{8}$$

where V_{L1} is the voltage at both ends of the inductor coil on the primary side. L_{P} is the excitation inductance of the primary side.

The reduction of magnetic flux in the core meets

$$\Delta\Phi_- = \frac{V_{L1}}{N_2} \cdot (t_3 - t_1)\,. \tag{9}$$

Since all of the energy in the leakage inductance is released into the capacitor C_2. The voltage V_{ds} on the D-S terminal at this stage can be expressed as

$$V_{ds} = V_{OR} + V_{B0} \tag{10}$$

where V_{OR} is the reflected voltage from the primary side to the secondary side of the transformer.

State IV (t_3 - t_4): all switches keep OFF.

During the period t_3-t_4, the circuit remains stationary without current flowing. C_{DS} and the secondary side inductor L_{S} form a low-frequency oscillation. The voltage V_{DS} is approximately equal to V_{B0}.

D. Analysis of the Circuit Loss

The losses of the circuit mainly include transformer winding loss P_{cu} and magnetic loss P_{core}, switches loss P_{SW}, and the loss P_{LK} caused by leakage inductance.

Winding loss in flyback transformers is mainly due to the proximity effect and skin effect. The winding excitation of the flyback transformer is a triangular wave with a phase difference of 110° between the fundamental components of the primary and secondary currents, which is different from the ideal transformer when calculating the winding losses. By a Fourier transform, the current is decomposed into an ideal transformer current component and an ideal inductor current component by orthogonal decomposition. Then according to the ideal transformer winding loss model [33], it can be obtained the winding loss of the flyback transformer can be expressed as

$$P_{cu} = P_T + P_{Lm} \tag{11}$$

where P_{T} is the loss caused by the transformer current component. P_{Lm} is the loss caused by the inductor current component.

According to the modified Steinmetz equation (MSE) model [34], [35], the transformer magnetic loss can be expressed as

$$P_{\mathrm{core}} = \mathrm{k} \cdot f \cdot {f_{eq}}^{\alpha-1} \cdot B_m^{\beta} \tag{12}$$

where B_{m} is the peak magnetic induction strength, and k, α, and β are frequency-dependent parameters that are generally given by the core manufacturer based on test data. f is the frequency of sinusoidal excitation. f_{eq} is the equivalent frequency in the case of non-sinusoidal excitation, which can be expressed as

$$f_{eq}=\frac{2}{\Delta B^2 \pi^2}\int_T \left(\frac{\mathrm{d}B}{dt}\right)^2 dt. \tag{13}$$

MOSFET loss P_{SW} mainly includes conduction loss, output capacitor charging and discharging loss, and switches loss [36], [37], which can be expressed as

$$P_{SW} = R_{\mathrm{DSON}} {I_{DS\mathrm{rms}}}^2 + \frac{1}{2} C_{\mathrm{DS}} {V_{\mathrm{DS}}}^2 \mathrm{f} + \mathrm{P}_{O\_F} \tag{14}$$

where P_{O_F} is the switched loss as

$$P_{O\_F} = \frac{1}{2}\left((\mathrm{t}_{D\_\mathrm{ON}} + t_r) + (\mathrm{t}_{D\_\mathrm{OFF}} + t_{\mathrm{f}})\right) V_{\mathrm{DS}} I_{\mathrm{DS}} f. \tag{15}$$

The loss P_{LK} consists of the energy stored by the leakage inductance P_{RCD} and the loss P_{OR} of the reflected voltage source on the core, which can be expressed as

$$P_{LK} = P_{\mathrm{RCD}} + P_{\mathrm{OR}} = \frac{1}{2} L_{LK} I_{L_{LK}}^2 \mathrm{f} \frac{V_{\mathrm{Clamp}}}{V_{\mathrm{Clamp}} - V_{\mathrm{OR}}}. \tag{16}$$

Based on the abovementioned analysis, equilibrium efficiency is defined as

$$\eta = \frac{P_O}{P_O + P_{\mathrm{cu}} + P_{\mathrm{core}} + P_{SW} + P_{LK}} \times 100\%. \tag{17}$$

III. DESIGN RULES FOR EQUALIZER

To design an equalizer with superior performance, parameters such as transformer winding turns ratio n, winding inductance, switching frequency f, duty cycle D, and core air gap δ must be considered. Because the proposed equalizer operates in discontinuous conduction mode (DCM) mode, the flux variation of the transformer needs to be zero in one switching cycle to ensure complete demagnetization, which can be expressed as

$$\Delta\Phi_{+}=\Delta\Phi_{-}. \tag{18}$$

Substituting (4), (9) into (18), the transformer turns ratio, winding voltage, and switching time meet

$$\frac{V_{L2}}{V_{L1}} = \frac{N_2}{N_1} \cdot \frac{t_1 - \mathrm{t}_0}{t_3 - t_1}. \tag{19}$$

1) Winding Turns Ratio n*:* In the core containing the air gap, the remanent magnetic flux density of the transformer is close to zero. In this case, the number of inductor turns meets

$$n = \frac{LI_{LK}}{A_{\mathrm{e}} B_{PK}}. \tag{20}$$

The calculated turns ratio n is the minimum value, the actual turns ratio must be larger than the calculated value, otherwise, the magnetic induction strength will be greater than 0.3 T, resulting in magnetic saturation. Meanwhile, the turns ratio of the coil should not be too large, otherwise, it will lead to a rapid increase in winding losses. When the low voltage terminal of the Battery Charger is set to 12 V, the primary and secondary winding voltages are about 1:4, thus setting the initial transformer turns ratio to 1:4.

2) Duty Cycle D*:* To ensure that the flyback converter is sufficiently demagnetized in one cycle. Equation (19) needs to be satisfied. With a transformer turns ratio of 1:4 and a primary and secondary voltage ratio of 1:4, the duty cycle D needs to be set to 50%. The circuit inevitably has various losses, in which case the equalizer will be in DCM mode.

3) Switching Frequency f: According to (3) and (8), the lower the switching frequency, the larger the equalization current. However, the transformer size becomes larger as the switching frequency decreases. The hysteresis loss and eddy current loss of the iron core increase when the frequency of the transformer increases, making the iron loss of the transformer higher. Usually, the switching frequency of the flyback converter is set between 20–100 kHz.

4) Winding Inductance: According to (3) and (8), the value of winding inductance will directly affect the magnitude of the equalization current. By reducing the winding inductance, a larger equalizing current can be obtained. But the winding inductance cannot be reduced all the time. Too small of the inductance value will result in the transformer not being able to store energy, making it less efficient. Under the above conditions of duty cycle D and switching frequency f, the transformer primary-side inductance is set to be 4 μH. The transformer turns ratio is 1:4, and the theoretical inductance of the secondary side is 64 μH.

5) Transformer Air Gap δ: In the process of designing the transformer, the inductance is usually controlled by changing the core air gap length. The inductance can be reduced by increasing the length. Similarly, the inductance can be increased by decreasing the air gap length. Usually, the operating state of the converter and the transformer turns ratio is not changeable at

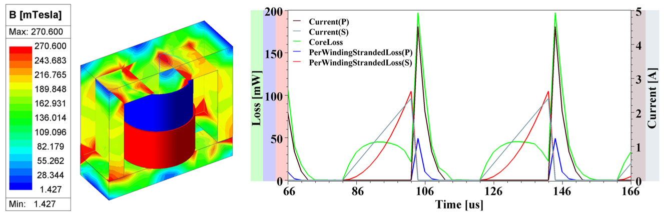

(a) (b)

Fig. 7. Transformer transient field finite element model. (a) Magnetic field strength distribution. (b) Transformer losses.

TABLE I
TRANSFORMER PARAMETERS

Parameter	Transformer T_1		Transformer T_2	
	P	S	P	S
$L_m(\mu H)$	4	65	4.3	70
$L_{eq}(\mu H)$	0.05	6	0.05	6.3
$R_{eq}(\mu H)$	0.072	2.25	0.075	2.58
N_p	4		4	
N_s	12		12	

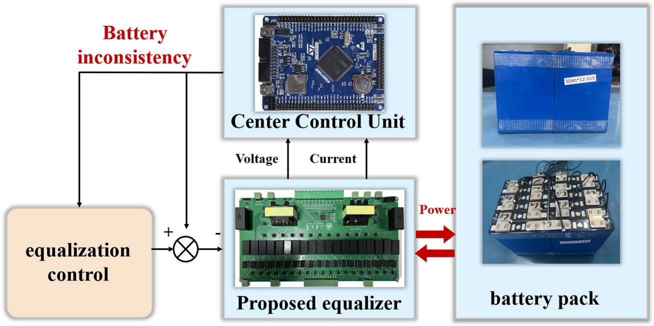

Fig. 8. Experimental prototype with 12 series-connected batteries.

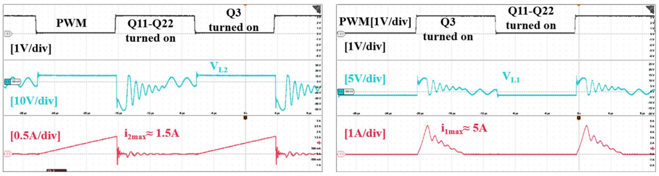

(a) (b)

Fig. 9. Battery cell charging experimental waveforms. (a) Secondary side waveform of the transform. (b) Primary side waveform of the transform.

will. The only feasible way to adjust the inductance is to change the air gap length. A large air gap length leads to a leakage flux rapidly increasing, which will higher the coil eddy current losses. On the contrary, when the air gap length is small, the machining accuracy requirement becomes high, which is not favorable to the design of the transformer. According to the design experience, the core air gap length is usually set between 0.1–1.5 mm.

Based on the analysis, a transient field finite element model of the flyback converter is built by Maxwell simulation software from Ansys. The transformer primary and secondary turn ratio is set to 1:4. Fig. 7(a) shows the transformer model. The maximum magnetic flux is 270 mT, which is less than the core saturation value. Fig. 7(b) illustrates the core loss and the losses in each winding of the transformer. It can be seen that the maximum magnetic loss is 0.2 W, which meets the theoretical calculations.

Table I gives the relevant parameters of the designed two transformers T_1 and T_2.

IV. EXPERIMENTAL RESULTS

An experimental prototype with 12 series-connected batteries is built to verify the effectiveness of the equalizer. The experimental platform is shown in Fig. 8. The experimental prototype includes an equalizer, a central control unit, and a series battery pack.

Switches Q_1–Q_6 in the equalizer are a single N-channel MOSFET, model WSP16N10, with an ON-resistance of 8.9 mΩ. The remaining MOSFET are two N-channel MOSFET, model WSP11N10T, with an ON-resistance of 70 mΩ. The withstand voltage of all MOSFET is 100 V. The relays K_1 and K_2 are selected from the small high-power dc relay HF115F. The voltage acquisition chip is XL8812, which can simultaneously collect twelve-channel voltage information and transmit it to the central control unit via SPI. The central control unit uses the STM32 microcontroller. According to the equalization strategy, the microcontroller outputs the corresponding PWM signals to control the MOSFET and relays. The battery used is a high-capacity lithium iron phosphate battery. The nominal voltage of the battery cell is 3.2 V and the nominal capacity is 30 Ah. The charging cut-off voltage is 3.65 V and the discharging cut-off voltage is 2.5 V.

A. Experimental Waveform Analysis

During the equalization process, the primary and secondary sides of the transformer conduct alternately. Particularly, according to the hardware schematic of the designed circuit, the low level of PWM drives the MOSFET on and the high level drives the MOSFET OFF. The circuit switching frequency is set to 50 kHz.

The charging waveforms are shown in Fig. 9. During the PWM low level, the secondary side switch Q_3 turns ON. The current i_2 on the secondary side of the transformer is established first and the current rises linearly. The secondary side voltage V_{L2} is approximately equal to the battery charger voltage 12 V. During the PWM high level, the primary side switches Q_{11}–Q_{22} turn ON. The primary side current i_1 decreases linearly from the maximum value. The battery cell starts to charge. The peak charging current is 5 A and the rms value of the current is approximately 2.45 A. The discharging waveforms are shown in Fig. 10. During the PWM low level, the primary side switches Q_{11}–Q_{22} turn ON. The current i_1 on the primary side of the transformer is established first and the current rises linearly. The battery cell starts to discharge. During the PWM high level, the secondary side switch Q_3 turns ON. The secondary side current i_2 decreases linearly from the maximum value. The peak discharge

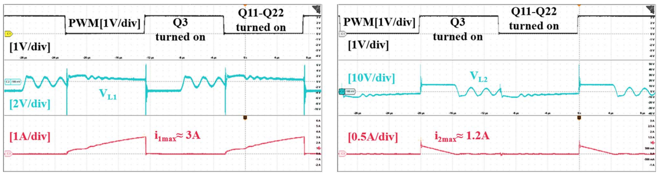

(a) (b)

Fig. 10. Battery cell discharging experimental waveforms. (a) Primary side waveforms of the transform. (b) Secondary side waveforms of the transform.

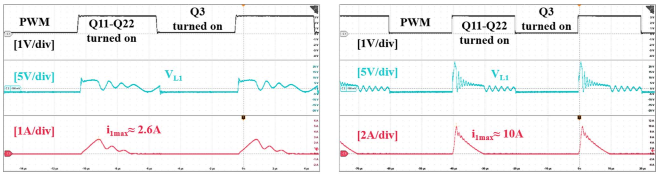

(a) (b)

Fig. 11. Equalization current waveforms at different frequencies. (a) Charging current at 100 kHz. (b) Charging current at 25 kHz.

current is 3 A and the rms value of the current is about 1.2 A. The experimental results show that the measured waveforms are in good agreement with the theoretical values.

B. Equalization Current at Different Frequencies

According to (8), the equalization current value is closely related to the circuit switching frequency. The parameters of the transformer are kept consistent with Table I. The secondary side of the transformer is connected to the 12 V low-voltage terminal of the battery charger. Figs. 11(a), (b), and 9(b), respectively, illustrate the equalized current waveforms at 100 kHz, 25 kHz, and 50 kHz switching frequencies. The peak equalization currents correspond to 2.6 A, 10 A, and 5 A. As the switching frequency decreases, the equalization current gradually increases, which is in good agreement with the theoretical values.

C. Voltage Equalization Results Analysis

To reduce the influence of the polarization reaction inside the cell during the equalization process on the experimental results, a certain resting time was set in the experiment. Here, the experiments are set for a resting time of 20 s. The initial distribution of cell voltages for the four tests is shown in Table II.

Three sets of experiments were conducted to see the equalization effect at different switching frequencies and different initial voltage distributions. Fig. 12(a) illustrates the equalization results at a maximum pressure difference of 196 mV and a switching frequency of 50 kHz. The equalization time is approximately 370 min, and the maximum pressure difference is 6 mV at the end of the equalization. Fig. 12(b) illustrates the equalization results at a maximum pressure difference of 80 mV and a switching frequency of 50 kHz. The equalization time is approximately 130 min, and the maximum pressure difference is 6 mV at the end of the equalization. Fig. 12(c) illustrates the equalization results at a maximum pressure difference of 84 mV and a switching frequency of 100 kHz. The equalization time is approximately 180 min, and the maximum pressure difference is 5 mV at the end of the equalization. It can be seen that the battery cells start charging and discharging from the cell with the largest voltage difference. As equalization proceeds, the battery pack voltage gradually converges. And the equalization time decreases gradually as the maximum voltage difference reduces and the switching frequency drops. The equalization effect is superior.

Fig. 13 illustrates the charging equalization results at a maximum voltage difference of 101 mV and a switching frequency of 50 kHz. At lower voltages, the battery pack is first charged through the high voltage of the battery charger. After reaching the charging threshold voltage, the single cell is then charged through the low voltage of the battery charger. All batteries can

TABLE II
INITIAL BATTERY VOLTAGE

	Test I Fig. 12 (a)	Test II Fig. 12 (b)	Test III Fig. 12 (c)	Test IV Fig. 13
B_1	2.898 V	3.007 V	3.008 V	3.413 V
B_2	2.910 V	3.009 V	3.015 V	3.424 V
B_3	2.929 V	3.039 V	3.039 V	3.428 V
B_4	2.949 V	3.044 V	3.045 V	3.434 V
B_5	3.010 V	3.044 V	3.049 V	3.440 V
B_6	3.016 V	3.050 V	3.050 V	3.441 V
B_7	3.017 V	3.054 V	3.055 V	3.447 V
B_8	3.021 V	3.061 V	3.062 V	3.450 V
B_9	3.045 V	3.061 V	3.067 V	3.450 V
B_{10}	3.074 V	3.065 V	3.069 V	3.456 V
B_{11}	3.076 V	3.076 V	3.080 V	3.474 V
B_{12}	3.094 V	3.087 V	3.092 V	3.514 V

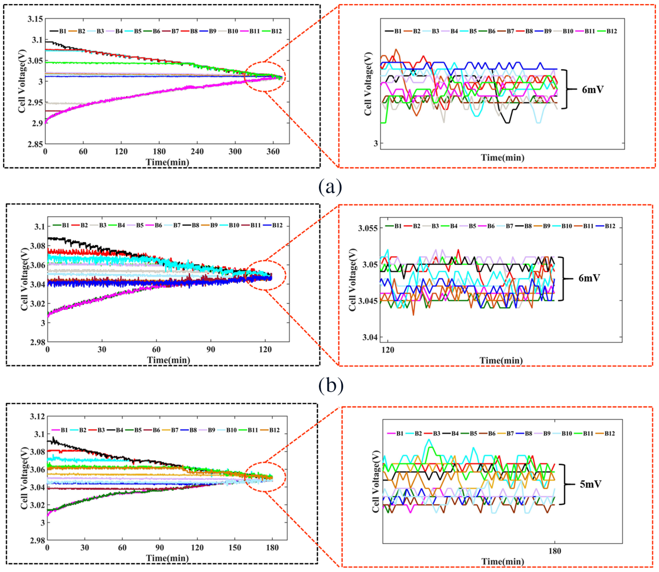

(a)

(b)

(c)

Fig. 12. Voltage waveform in equalization mode. (a) Maximum differential pressure 196 mV, frequency 50 kHz. (b) Maximum differential pressure 80 mV, frequency 50 kHz. (c) Maximum differential pressure 84 mV, frequency 100 kHz.

TABLE III
COMPARISON OF SEVERAL EXISTING EQUALIZERS

Equalizers	Components				Equalization current	Circuit cost	Circuit compactness	Control simplicity	Equalization speed
	SW	L	C	T					
Capacitor [20]	$2n$	0	n	0	0.9 A	Medium	Medium	High	Low
Inductor [24]	$2n$-2	$n/2$	0	0	1.5 A	Medium	Medium	Medium	Medium
Two-Stage charge equalizer [29]	$4n$+2	0	0	2	0.2 A	High	Low	Low	Low
Multiwinding transformer [30]	n	0	n	x	1.1 A	Low	High	Medium	Medium
Multiwinding transformer [31]	n	0	0	x	0.1 A	Low	High	Medium	Low
Flyback converter [32]	$4n$+4	0	0	x	2.4 A	High	Low	High	Medium
Proposed equalizer	$2n$+8	0	0	2	5.0 A	Low	High	High	High

n is the number of cells in the battery pack. x is the number of battery modules in the battery string. SW: MOSFET switches. L: Inductors. C: Capacitors. T: Transformers.

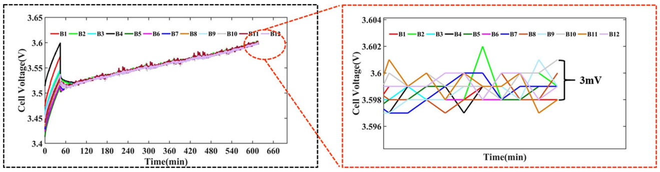

Fig. 13. Voltage waveform in charge equalization mode.

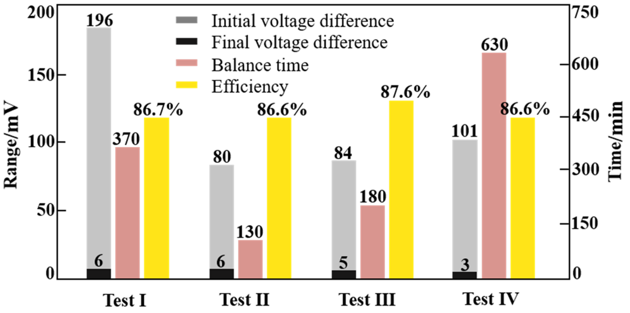

Fig. 14. Statistical results of experiments under different conditions.

reach 3.6 V at the end of charge equalization, which greatly increases the usable capacity of the battery pack.

Fig. 14 illustrates the results of the four sets of experiments. It can be seen that after the equalization, the maximum pressure difference of the battery pack is less than 6 mV with good consistency. Moreover, while ensuring large current equalization, there is a high equalization efficiency up to 87%.

V. COMPARISON WITH EXISTING EQUALIZERS

Table III illustrates the comparison of the proposed equalizer with the existing equalizer. The comparison includes the number of various electrical components required for the equalizer to perform its function and the equalization current. The indicators of circuit cost, compactness, control simplicity, and equalization speed were also evaluated. The various indicator scores are categorized as high, medium, and low from best to worst.

It is worth mentioning the comparison in terms of equalization current. In capacitor-based circuits, the larger the capacity of the condenser, the faster the charge transfer, and the larger the current. However, it will lead to an increase in the size of the circuit. Typically, the current of capacitor-based equalization circuits is in the range of tens to hundreds of milliamps. In circuits based on inductors and transformers, by decreasing the inductance value or increasing the switching frequency, the theoretical current can be increased in this type of topology. However, as the inductance value decreases, the inductor may no longer exhibit inductance. Also, as the switching frequency gradually increases, the circuit losses gradually increase. Usually, equalization current is limited by a number of factors such as circuit size and cost. It is the result of a combination of various variables. In order to be closer to the engineering reality, the circuit size, cost, and efficiency are combined to calculate the current when the equalizer works optimally.

The equalization topologies based on capacitors and inductors proposed in [20] and [24] tend to require a large number of switching devices and energy storage elements, which leads to a high circuit cost and low circuit compactness. It is worth mentioning that the equalization topology in [20] does not require additional voltage monitoring circuits to achieve automatic equalization, which is simple to control. The modular two-stage charge equalization topology proposed in [29] achieves equalization with greatly reduced voltage stresses on the electrical components. However, it requires a large number of switching devices, which makes the circuit cost high and the control complex. Distinguishing from the capacitor and inductor equalization methods, the equalization topology based on the multiwinding transformer proposed in [30] and [31] requires only one switch control for each cell, with lower cost and high circuit compactness. However, the fabrication of the multiwinding transformer and its control process are very complicated. Meanwhile, the circuit design is not reasonable resulting in a small equalization current and low equalization speed. The equalization topology based on flyback conversion proposed in [32] achieves large current equalization without an additional degaussing circuit. However, ($4n$+4) switches are required leading to a large circuit size. From the table, it can be seen that the past equalizers have been somewhat flawed to varying degrees.

The proposed equalizer requires only $(2n+8)$ switches and two transformers, without additional inductors and capacitors. By comparing with [32], it can be seen that about half of the MOSFETs are reduced, which greatly reduces the cost and improves the compactness of the circuit. Moreover, the maximum equalization current rms of the circuit is as high as 2.4 A, which is much better than the previous equalizer. Equalization speed has been greatly improved, making it more suitable for equalizing large battery packs. In conclusion, the proposed equalizer has the advantages of low cost, small size, simple control, and fast equalization at the same time, which is a superior performance equalizer.

VI. CONCLUSION

In this article, a compact equalizer with a large current based on flyback conversion for large battery packs is proposed. First, the different types of existing equalization topologies are described. Then, the working principle of the proposed equalization topology is explained. And analyzed the experimental waveforms under different working conditions. Subsequently, a 12-cell series battery pack experimental platform was built to verify the feasibility of the circuit topology. The experimental results show the proposed equalizer has the following superior performance.

1) By sharing the MOSFETs array, the equalizer reduces the number of switching devices by about 50%.
2) By rationally designing the converter, large-current equalization is realized. The equalization speed is improved, which is suitable for large battery packs.
3) The equalizer has both equalization and charge equalization modes, achieving the effect of a dual-purpose machine.

To improve the applicability of the topology, in our future work it will be explored to optimize the circuit structure. The cell-to-module and module-to-module equalization will be designed, continuing to improve the equalization speed.

REFERENCES

[1] Z. G. Yang, J. L. Zhang, K.-M. Michael, and X. C. Lu, "Electrochemical energy storage for green grid," *Chem. Rev.*, vol. 111, no. 5, pp. 3577–3613, Jun. 2011.

[2] Z. Mao, X. Gu, J. Li, K. Liu, T. Wang, and Y. Shang, "An applicable minor short-circuit fault diagnosis method for automotive lithium-ion batteries based on extremum sample entropy," *IEEE Trans. Power Electron.*, vol. 39, no. 4, pp. 4636–4644, Apr. 2024.

[3] Z. Wei, F. Peng, and H. Wang, "An LCC-based string-to-cell battery equalizer with simplified constant current control," *IEEE Trans. Power Electron.*, vol. 37, no. 2, pp. 1816–1827, Feb. 2022.

[4] Y. Shang, N. Cui, B. Duan, and C. Zhang, "Analysis and optimization of star-structured switched-capacitor equalizers for series-connected battery strings," *IEEE Trans. Power Electron.*, vol. 33, no. 11, pp. 9631–9646, Nov. 2018.

[5] T. Wang et al., "Capacity multistage degradation analysis and knee point prediction method of lithium-ion battery," *Green Energy Intell. Transp.*, vol. 3, no. 5, 2024, Art. no. 100171.

[6] F. Peng, Y. Lu, M. Zhou, and H. Wang, "Hierarchical modular battery equalizer with open-loop control and mitigated recovery effect," *CPSS Trans. Power Electron. Appl.*, vol. 6, no. 4, pp. 310–319, Dec. 2021.

[7] M. Uno and A. Kukita, "String-to-battery voltage equalizer based on a half-bridge converter with multistacked current doublers for series-connected batteries," *IEEE Trans. Power Electron.*, vol. 34, no. 2, pp. 1286–1298, Feb. 2019.

[8] Y. Wang, Y. Shang, X. Gu, J. Li, and C. Zhang, "An incipient multi-fault diagnosis method for lithium-ion battery pack based on data-driven with incremental-scale," *IEEE Trans. Transp. Electrific.*, to be published, doi: 10.1109/TTE.2024.3363238.

[9] C. Hua and Y.-H. Fang, "A charge equalizer with a combination of APWM and PFM control based on a modified half-bridge converter," *IEEE Trans. Power Electron.*, vol. 31, no. 4, pp. 2970–2979, Apr. 2016.

[10] B. Duan, Z. Y. Li, P. W. Gu, Z. K. Zhou, and C. H. Zhang, "Evaluation of battery inconsistency based on information entropy," *J. Energy Storage*, vol. 16, pp. 160–166, Apr. 2018.

[11] Y. J. Zheng, W. K. Gao, and M. G. Ouyang, "State-of-charge inconsistency estimation of lithium-ion battery pack using mean-difference model and extended Kalman filter," *J. Power Sources*, vol. 383, pp. 50–58, Dec. 2018.

[12] H. Zhang, Y. Wang, H. Qi, and J. Zhang, "Active battery equalization method based on redundant battery for electric vehicles," *IEEE Trans. Veh. Technol.*, vol. 68, no. 8, pp. 7531–7543, Aug. 2019.

[13] Y. Chen, X. Liu, Y. Cui, J. Zou, and S. Yang, "A multiwinding transformer cell-to-cell active equalization method for lithium-ion batteries with reduced number of driving circuits," *IEEE Trans. Power Electron.*, vol. 31, no. 7, pp. 4916–4929, Jul. 2016.

[14] X. Qi, M. Fang, Y. Wang, Y. Wang, and Z. Chen, "An equalization current ripple cancellation (ECRC) converter-based centralized equalization system for series-connected battery strings," *IEEE Trans. Transp. Electrific.*, vol. 9, no. 2, pp. 2765–2777, Jun. 2023.

[15] J. Nie, R. Fu, C. Cai, J. Ma, Z. Shu, and L. Ma, "A high efficiency battery equalizing circuit based on half bridge topology with multiport transformer," *IEEE Trans. Ind. Electron.*, vol. 71, no. 3, pp. 2522–2532, Mar. 2024.

[16] S. Wang, Y. Wang, G. Chen, D. Wei, and Y. Shang, "An efficient and compact equalizer based on forward-flyback conversion for large-scale energy storage systems," *IEEE Trans. Transp. Electrific.*, vol. 10, no. 1, pp. 1222–1232, Mar. 2024.

[17] Y. Shang, C. Zhang, N. Cui, and C. C. Mi, "A delta-structured switched-capacitor equalizer for series-connected battery strings," *IEEE Trans. Power Electron.*, vol. 34, no. 1, pp. 452–461, Jan. 2019.

[18] K. Liu, Z. Yang, X. Tang, and W. Cao, "Automotive battery equalizers based on joint switched-capacitor and buck-boost converters," *IEEE Trans. Veh. Technol.*, vol. 69, no. 11, pp. 12716–12724, Nov. 2020.

[19] H. Chen, "A simple and effective capacitor-based equalizer for cell-to-cell battery equalization," *Int. J. Circuit Theory Appl.*, vol. 52, no. 4, pp. 1666–1681, Apr. 2024.

[20] Y. Shang, B. Xia, F. Lu, C. Zhang, N. Cui, and C. C. Mi, "A switched-coupling-capacitor equalizer for series-connected battery strings," *IEEE Trans. Power Electron.*, vol. 32, no. 10, pp. 7694–7706, Oct. 2017.

[21] X. Guo, Q. Wu, C. Xing, W. Qian, and W. Cao, "An active equalization method based on an inductor and a capacitor for series battery pack," *IEEE Trans. Power Electron.*, vol. 38, no. 3, pp. 4040–4052, Mar. 2023.

[22] S.-W. Lee, K.-M. Lee, Y.-G. Choi, and B. Kang, "Modularized design of active charge equalizer for li-ion battery pack," *IEEE Trans. Ind. Electron.*, vol. 65, no. 11, pp. 8697–8706, Nov. 2018.

[23] X. Ding et al., "A novel active equalization topology for series-connected lithium-ion battery packs," *IEEE Trans. Ind. Appl.*, vol. 56, no. 6, pp. 6892–6903, Nov./Dec. 2020.

[24] C. Lu, L. Kang, S. Wang, Z. Wang, and H. Rao, "A novel inductor-based non-dissipative equalizer," *Energies*, vol. 11, no. 10, Oct. 2018, Art. no. 2816.

[25] Y. Li, J. Xu, X. Mei, and J. Wang, "A unitized multiwinding transformer-based equalization method for series-connected battery strings," *IEEE Trans. Power Electron.*, vol. 34, no. 12, pp. 11981–11989, Dec. 2019.

[26] R. Mai, B. Xu, Z. Yan, W. Zhou, and L. Liu, "A compact-size multi-winding transformer-based discharge equalizer for electric two-wheelers and three-wheelers vehicles power battery," *IEEE Trans. Veh. Technol.*, vol. 71, no. 5, pp. 4889–4897, May 2022.

[27] B. Xu et al., "Modularized equalization architecture with transformer-based integrating voltage equalizer for the series-connected battery pack in electric bicycles," *IEEE Trans. Ind. Electron.*, vol. 70, no. 7, pp. 6984–6992, Jul. 2023.

[28] Y. Shang, N. Cui, B. Duan, and C. Zhang, "A global modular equalizer based on forward conversion for series-connected battery strings," *IEEE J. Emerg. Sel. Topics Power Electron.*, vol. 6, no. 3, pp. 1456–1469, Sep. 2018.

[29] C.-H. Kim, M.-Y. Kim, H.-S. Park, and G.-W. Moon, "A modularized two-stage charge equalizer with cell selection switches for series-connected lithium-ion battery string in an HEV," *IEEE Trans. Power Electron.*, vol. 27, no. 8, pp. 3764–3774, Aug. 2012.

[30] S. Li, C. C. Mi, and M. Zhang, “A high-efficiency active battery-balancing circuit using multiwinding transformer,” *IEEE Trans. Ind. Appl.*, vol. 49, no. 1, pp. 198–207, Jan./Feb. 2013.

[31] Y. Shang, B. Xia, C. Zhang, N. Cui, J. Yang, and C. Mi, “A modularization method for battery equalizers using multiwinding transformers,” *IEEE Trans. Veh. Technol.*, vol. 66, no. 10, pp. 8710–8722, Oct. 2017.

[32] K. Yu, Y. Shang, X. Wang, N. Wang, B. Duan, and C. Zhang, “A multi-cell-to-multi-cell equalizer for series-connected batteries based on flyback conversion,” in *Proc. 3rd Conf. Veh. Control Intell.*, 2019, pp. 1–5.

[33] Z. Lu and W. Chen, “Novel winding loss analytical model of flyback transformer,” in *Proc. 37th IEEE Power Electron. Specialists Conf.*, 2006, pp. 1–6.

[34] M. Albach, T. Durbaum, and A. Brockmeyer, “Calculating core losses in transformers for arbitrary magnetizing currents a comparison of different approaches,” in *Proc. 27th Annu. IEEE Power Electron. Specialists Conf.*, 1996, vol. 2, pp. 1463–1468.

[35] J. Reinert, A. Brockmeyer, and R. W. A. A. De Doncker, “Calculation of losses in ferro- and ferri-magnetic materials based on the modified Steinmetz equation,” *IEEE Trans. Ind. Appl.*, vol. 37, no. 4, pp. 1055–1061, Jul./Aug. 2001.

[36] A. Anurag, S. Acharya, and S. Bhattacharya, “An accurate calorimetric loss measurement method for SiC MOSFETs,” *IEEE J. Emerg. Sel. Topics Power Electron.*, vol. 8, no. 2, pp. 1644–1656, Jun. 2020.

[37] U. Jadli, F. Mohd-Yasin, H. A. Moghadam, P. Pande, J. R. Nicholls, and S. Dimitrijev, “Measurement of power dissipation due to parasitic capacitances of power MOSFETs,” *IEEE Access*, vol. 8, pp. 187043–187051, 2020.

Shiquan Liu received the B.S. degree in automation from Qingdao University, Qingdao, China, in 2022. He is currently working toward the M.S. degree in control science and engineering with the School of Control Science and Engineering, Shandong University, Jinan, China.

His research interests include battery balancing and battery charging.

Yue Wang (Graduate Student Member, IEEE) received the M.E. degree in electrical engineering from Qingdao University, Qingdao, China, in 2019. He is currently working toward the Ph.D. degree in control science and engineering with the School of Control Science and Engineering, Shandong University, Jinan, China.

His research interests include battery safety, efficient utilization, and battery management system design.

Shiyu Wang received the B.S. degree in automation from Shandong University, Jinan, China, in 2021. He is currently working toward the M.E. degree in control science and engineering with the School of Control Science and Engineering, Shandong University, Jinan, China.

His research interests include battery balancing and battery charging and heating.

Wenyuan Zhao received the B.S. degree in automation from the Qingdao University, Qingdao, China, in 2021. He is currently working toward the M.S. degree in control engineering with the School of Control Science and Engineering, Shandong University, Jinan, China.

His research interests include the optimization of lithium-ion battery fast charging and the design of battery management system.

Yunlong Shang (Member, IEEE) received the B.S. degree in automation from the Hefei University of Technology, Hefei, China, in 2008, and the Ph.D. degree in control theory and control engineering from Shandong University, Jinan, China, in 2017.

In 2019, he was with Shandong University, where he is currently a Professor with the School of Control Science and Engineering. Between 2015 and 2017, he conducted scientific research as a Joint Ph.D. Student with the Department of Electrical and Computer Engineering, San Diego State University, USA, where between 2017 and 2019, he was a Postdoctoral Research Fellow. His current research interests include battery balancing, battery modeling and states estimation, self-heating for low-temperature batteries, and design of battery management systems.

Dr. Shang was the recipient of the outstanding paper award of IEEE TRANSACTIONS ON INDUSTRIAL ELECTRONICS in 2022.